JOURNAL OF PROPULSION AND POWER
Vol. 13, No. 6, November–December 1997

Numerical Analysis of a Two-Dimensional Magnetoplasmadynamic Arcjet

I. Funaki,* K. Toki,† and K. Kuriki‡
Institute of Space and Astronautical Science, Sagamihara, Kanagawa 229, Japan

The effect of electrode configuration on thrust characteristics of a two-dimensional magnetoplasmadynamic (MPD) arcjet was numerically investigated. A simple magnetohydrodynamics (MHD) model was developed and the numerical results were compared with the experimental data for several electrode geometries. To understand the features of the flowfield, we introduced a magnetosonic Mach number, which is defined as local velocity divided by a propagation speed of the MHD disturbance. Based on the magnetosonic Mach number distribution of the flowfield, the model can explain the thrust characteristics of the MPD arcjet, especially the superiority of a short cathode under various anode configurations. Because the electromagnetic thrust is unaltered for the same anode configuration, the electrothermal component of thrust makes a difference between the long and the short cathodes. With a short cathode configuration, the large heat deposition near the cathode tip, which is inevitable to MPD arcjets, can be confined in the submagnetosonic region where the local flow is accelerated to magnetosonic velocity. Then the thermal deposition into the submagnetosonic region can be efficiently recovered through transmagnetosonic acceleration, resulting in a large thrust generation.

Nomenclature

a = sonic velocity
a_m = magnetosonic velocity
B, $\mathbf{B}$ = self-induced magnetic field
B_0 = inlet self-induced magnetic field
E = electric field
e = electricity
e_t = specific energy
Isp = specific impulse
J = total discharge current
j, $\mathbf{j}$ = current density
k = Boltzmann's constant
M_m = magnetosonic Mach number
$\dot{m}$ = mass flow rate
n_e = electron number density
p = pressure
R = gas constant
T = temperature
t = time
u, $\mathbf{u}$ = velocity, (u, v)
u_0 = inlet velocity
W = chamber width
x = coordinate
y = coordinate
γ = specific heat
ε_0 = permittivity in vacuum
μ_0 = permeability in vacuum
ρ = mass density
σ = electrical conductivity

Introduction

MANY theoretical activities have been underway in the research of magnetoplasmadynamic (MPD) arcjet, using direct simulations of the flowfield in the discharge chamber.[1–8] Most of the works target the complex physical aspects of the MPD arcjet: they include all probable physical phenomena such as electromagnetic acceleration, nenequilibrium ionization, temperature deviation of different species, and diffusion or viscous effects, mainly involved as the loss mechanism of MPD arcjet. Because of analytical simplicity, many investigators employed a one-dimensional model, as summarized by Niewood and Martinez-Sanchez et al.[5] Some of them were extended to two-dimensional analyses, including such effects as viscosity,[6] the Hall effect,[7] multiple ionization,[8] etc. Because the MPD arcjet shows poor performance at this stage as a result of its loss dominant feature, evaluating loss mechanisms in the discharge process is important to predict and improve thrust performance. In spite of these intensive researches to analyze these processes, performance prediction by a numerical model is very difficult. This is mainly caused by its poor ability to estimate discharge voltages, resulting in an overestimation of thrust performance, which is defined as the kinetic power over the total input power. This poor prediction of voltage comes from incomplete modeling of electrical conductivity or the inaccuracy of incorporating kinetic processes. Finally, there is the large energy deposition onto electrodes or the sheath region to be taken into account. In the study of MPD arcjets, it is advisable to be independent of such realistic analyses and to seek a good acceleration pattern based on the ideal magnetohydrodynamic (MHD) equations to obtain global insight for better MPD arcjet design guidelines. This includes neither complex reactive nor dissipative processes, but includes the thrust generation processes of both electromagnetic and thermodynamic acceleration.

Major objectives of the present analyses are to give insight into the following important questions:

1) Whether or not the thermal contribution is effective in thrust generation.

2) What kind of thruster configuration enhances thrust production.

3) When a short cathode configuration is adopted, pumping compression near the cathode tip may induce an oblique shock wave. Does it spoil the thermal thrust generation?

Our previous paper[9] indicated a design guideline for chamber geometry and propellant species of MPD arcjets, and suggested that in the enhancement of electrothermal thrust, adopting a short cathode configuration was the best choice for the

---

Received Oct. 23, 1997; revision received May 27, 1997; accepted for publication June 20, 1997.

*Researcher, Space Propulsion Division. Member AIAA.

†Associate Professor, Space Propulsion Division. Member AIAA.

‡Professor, Space Propulsion Division. Fellow AIAA.

Isp range below 3000 s. To support this result, plasma flow near the cathode tip is analyzed by two-dimensional MHD equations. In this simulation, different from an axisymmetrical model, a strict two-dimensional model was adopted; this facilitated the calculated results to be compared with the experimental results of a multichannel two-dimensional MPD arcjet (2D–MPD). Details of the 2D–MPD system and experimental data are available elsewhere.[9–11] The 2D–MPD approximates a two-dimensional plasma flowfield so that its side image can be directly observed and converted into plasma distributions such as electron temperature, plasma density, and magnetic field strength. Those data are ready to be compared with numerical results of not only the thrust performance, but also the flowfield in the discharge chamber.

Numerical Model

Assumptions

The following conditions were assumed to analyze the thrust generation mechanism of the 2D–MPD. Judging from optical images of the 2D–MPD arcjet's discharge chamber, only partial local thermodynamic equilibrium is applicable, except for the rarefied region outside the discharge chamber or the region near the electrode boundary. If the deviation from the complete local thermodynamic equilibrium is negligible, the following assumptions can be made. The efforts must be focused on the acceleration process of the main flow off the electrode boundaries; hence, both the electromagnetic and the gasdynamic boundary phenomena are not taken into account in this simulation.

1) Plasma flow is strictly two dimensional (2D–MPD approximates plasma flow by using eight discharge channels to secure the optical depth and to avoid nonuniform discharge along the line-of-sight). Only steady-state flow is of interest (2D–MPD is operated in a quasisteady mode).

2) Self-induced magnetic field is of interest, the Hall effect is neglected.

3) Argon is specified as propellant gas and fed into the chamber as fully ionized plasma, namely, it is treated as a single-fluid, quasineutral, and perfect gas.

4) Viscosity, thermal conductivity, electrical sheath, and radiation processes are neglected.

5) Electrical conductivity is given by the Spitzer–Härm's formulation, as an isotropic function of both density and temperature.

6) The plasma flow is accelerated from submagnetosonic speeds to supermagnetosonic speeds, where the magnetosonic speed is defined as

$$a_m = \sqrt{\gamma RT + (B_0^2/2\rho\mu_0)} \tag{1}$$

which is the propagating speed of small disturbances in the MHD flowfield. Using a_m, the magnetosonic Mach number is derived as

$$M_m = |\mathbf{u}|/a_m \tag{2}$$

Governing Equations

To use a time-marching algorithm, time-dependent equations are treated. In the MHD framework, the displacement current in the Maxwell equations is neglected. The basic electromagnetic equations are as follows.

Maxwell equations:

$$\frac{\partial \mathbf{B}}{\partial t} = -\mathrm{rot}\,\mathbf{E} \tag{3}$$

$$\mathbf{j} = (1/\mu_0)\mathrm{rot}\,\mathbf{B} \tag{4}$$

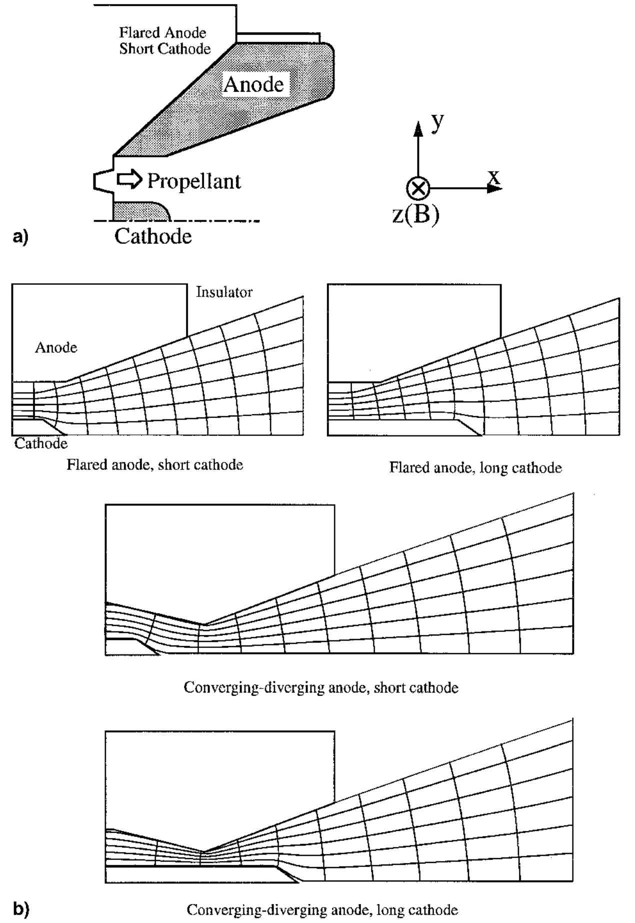

Flared anode, short cathode

Flared anode, long cathode

Converging-diverging anode, short cathode

Converging-diverging anode, long cathode

Fig. 1 Cross-sectional geometry of electrodes of two-dimensional MPD arcjet and its calculation grids: a) cross-sectional geometry of two-dimensional MPD arcjet and b) calculation grids.

Ohm's law:

$$j = \sigma(\mathbf{E} + \mathbf{u} \times \mathbf{B}) \tag{5}$$

Solving Eqs. (3–5) for the magnetic flux density, yields the induction equation

$$\frac{\partial \mathbf{B}}{\partial t} = \mathrm{rot}\left(\mathbf{u} \times \mathbf{B} - \frac{1}{\sigma\mu_0}\mathrm{rot}\,\mathbf{B}\right) \tag{6}$$

As for fluid equations, the Lorentz force term for the equation of motion and the Joule heating for the energy equation are taken into account. The inviscid Euler equations with electromagnetic source terms are as follows.

Mass conservation:

$$\frac{\partial \rho}{\partial t} + \nabla(\rho\mathbf{u}) = 0 \tag{7}$$

Equation of motion:

$$\frac{\partial \rho\mathbf{u}}{\partial t} + \nabla(\rho\mathbf{u}\mathbf{u} + p) = \mathbf{j} \times \mathbf{B} \tag{8}$$

Energy conservation:

$$\frac{\partial e_t}{\partial t} + \nabla\cdot[(e_t + p)\mathbf{u}] = \mathbf{j}\cdot\mathbf{E} \tag{9}$$

Equation of state:

$$p = \rho R T \tag{10}$$

All of the simulations were executed for the 2D-MPD arcjet. A cross-sectional view of the flared anode configuration was depicted in Fig. 1a. When applying the MHD equations for the Cartesian coordinates indicated in Fig. 1, the governing equations for flow variables can be transformed into a vectorized form

$$\frac{\partial}{\partial t}\begin{bmatrix}\rho\\ \rho u\\ \rho v\\ e_t\end{bmatrix}+\frac{\partial}{\partial x}\begin{bmatrix}\rho u\\ \rho u^2+p\\ \rho uv\\ (e_t+p)u\end{bmatrix}+\frac{\partial}{\partial y}\begin{bmatrix}\rho v\\ \rho uv\\ \rho v^2+p\\ (e_t+p)v\end{bmatrix}$$

$$=\begin{bmatrix}0\\ j_yB\\ -j_xB\\ j_xE_x+j_yE_y\end{bmatrix} \tag{11}$$

where

$$e_t=\frac{p}{\gamma-1}+\frac{1}{2}\rho u^2+\frac{1}{2}\rho v^2$$

is total energy. For the magnetic flux density, a scalar equation is derived:

$$\frac{\partial B}{\partial t}+\frac{\partial uB}{\partial x}+\frac{\partial vB}{\partial y}-\frac{\partial}{\partial x}\left(\frac{1}{\sigma\mu_0}\frac{\partial B}{\partial x}\right)-\frac{\partial}{\partial y}\left(\frac{1}{\sigma\mu_0}\frac{\partial B}{\partial y}\right)=0 \tag{12}$$

Equations (11) and (12) govern the plasma flow inside the chamber of the 2D-MPD.

The electrical conductivity was given by the Spitzer-Härm formulation, which was derived under the assumption of fully ionized plasma. It depends on both temperature and density as

$$\sigma = 1.5\times 10^{-2}\,(T^{3/2}/\ell n\,\Lambda) \tag{13}$$

where

$$\ell n\,\Lambda=\ell n\left[\frac{12\sqrt{2}\pi\varepsilon_0^{3/2}}{e^3}\frac{(kT)^{3/2}}{n_e^{1/2}}\right]$$

is the Coulomb logarithm.

Calculation Procedure

Grid Formation

Boundary-fitting coordinates perpendicular and parallel to boundary walls were created by solving the Laplace's equation, with which boundary conditions can accurately and easily be applied.[12] Practical simulations were executed after transforming the governing equations from physical space (x, y) into a rectangular calculation space without losing the strong conservation property of the Euler equation; and hence, the calculation scheme will not violate the conservation laws.

Figure 1b shows the calculation grids used for comparison with the experimental data. At the anode end, the supersonic flow forms a jet separating from the anode boundary, where the inviscid model fails. To avoid this difficulty, the rapid expansion region at the anode end was replaced by an insulator under the assumption that the flow near the anode end will not affect the core flow between the electrodes. Furthermore, the cathode tip geometry was also approximated by a linear function, because the hemispheric cathode geometry is difficult to treat when supersonic expansion is encountered.

Solver

Both the flow and the electromagnetic equations were discretized based on the finite difference method: for the Euler equation (11), the total variation diminishing (TVD)-MacCormack scheme with Roe-Davis's dissipation term was employed[13]; for the induction equation (12), all derivatives were discretized using the central differencing method and solved by the successive over relaxation method, dropping the time-dependent term because only the steady-state solution is of interest. Solving both equations alternatively and coupling them together, a steady solution was obtained.

With a numerical solution, thrust was evaluated from $\dot{m}u_{\text{exit}}$, using the mean exit velocity u_{exit}. The discharge voltage was also evaluated from the solution. With the magnetic flux den-

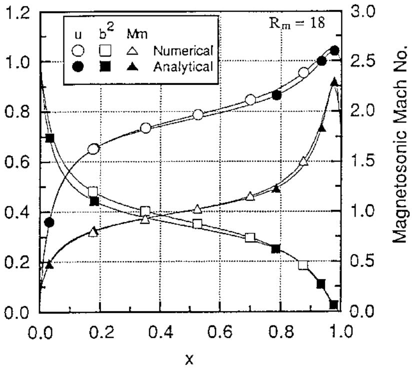

Fig. 2 Comparison between analytical and numerical solutions of one-dimensional flow; the analytic solution was obtained by King,[14] the conductivity is constant, and the magnetic Reynold's number is 18.

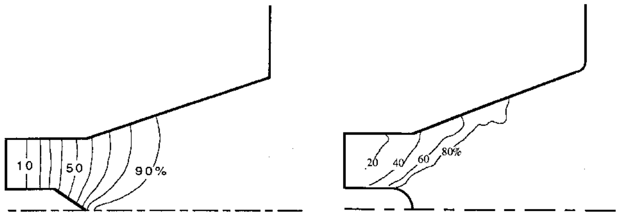

Calculation Experiment

Current contours

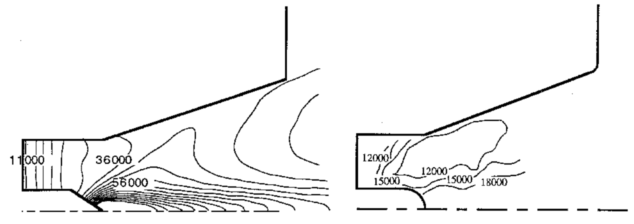

Calculation Experiment (Ref.11)

Temperature distribution, K

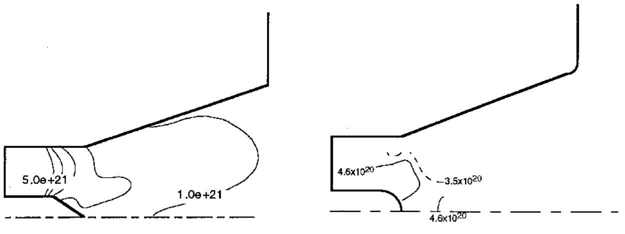

Calculation Experiment

Plasma density distribution, /m^3

Fig. 3 Flow near the cathode tip; current contours, temperature, and plasma density distribution, flared anode, short cathode, $\dot{m}$ = 1.25 g/s, and J = 12 kA.

sity distribution obtained, one can calculate discharge voltage by integrating the local electrical field along the current path.

Boundary Conditions

Electromagnetic boundary conditions were specified as follows. At the electrode surfaces, the tangential electric field component was fixed as zero, which forces the electrode surface to be an equipotential contour. At the inlet, the magnet flux density B_0 was given. In the case of the 2D-MPD, B_0 is related to J as

$$B_0 = \mu_0 J/2W \qquad (14)$$

where W is the channel width of the 2D-MPD. At other boundaries, i.e., outside the chamber, at the symmetry axis, and at the outlet boundary, the magnetic flux was set to zero.

Other boundary conditions for the flow variables are explained. The electrodes and the insulator were treated as slip walls. The subsonic inflow and supersonic outflow were specified for the inlet and the outlet boundary conditions. This means smooth acceleration from subsonic to supersonic velocity. Although this condition does not necessarily match the submagnetosonic condition of the inflow, it was adopted because the TVD scheme cannot directly deal with the magnetosonic velocity as a result of restrictions of the scheme for the flow equation (11). The subsonic inlet condition acts as a stronger constraint than a submagnetosonic inlet condition, because $u_0 < a < a_m$.

To realize the subsonic inflow, the mass flow rate and temperature were fixed, and density was extrapolated from the calculation region. In this simulation, the inlet temperature was assumed to be 5000 K. At the outflow, all variables were determined by zeroth order extrapolation. For the symmetry axis

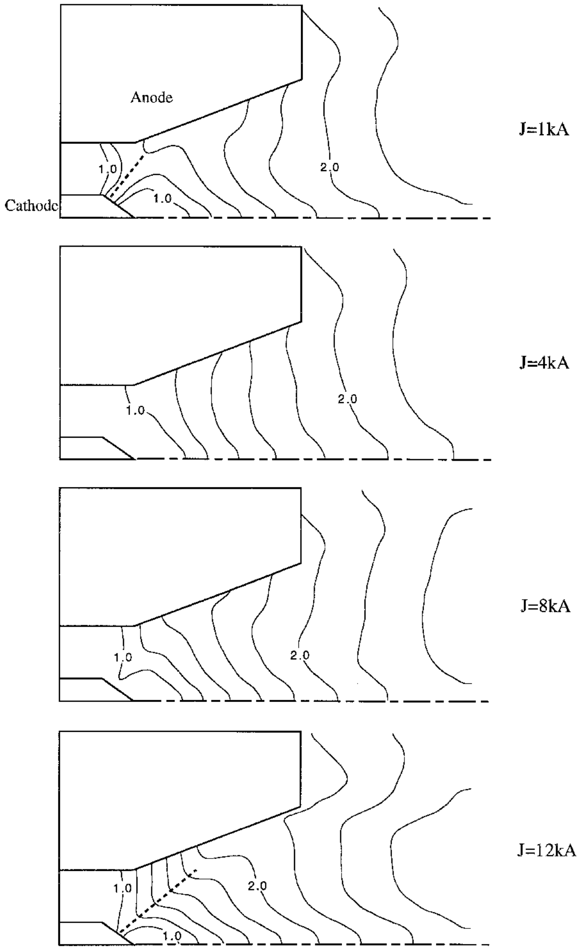

Fig. 4 Calculated magnetosonic Mach number distribution; the magnetosonic line detaches from the cathode tip at moderate discharge current, flared anode, and short cathode, $\dot{m}$ = 2.5 g/s.

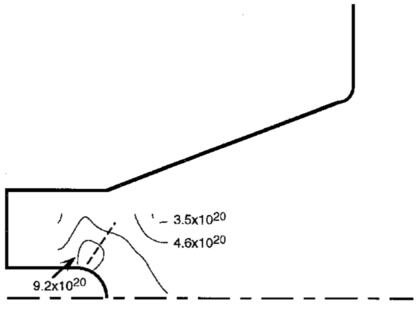

Experiment

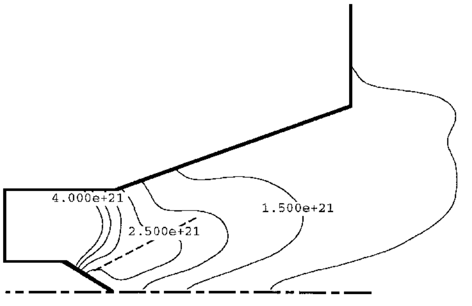

Calculation

Fig. 5 Plasma density profile near the cathode tip; measured and calculated plasma density profile (J = 16 kA, $\dot{m}$ = 2.5 g/s).

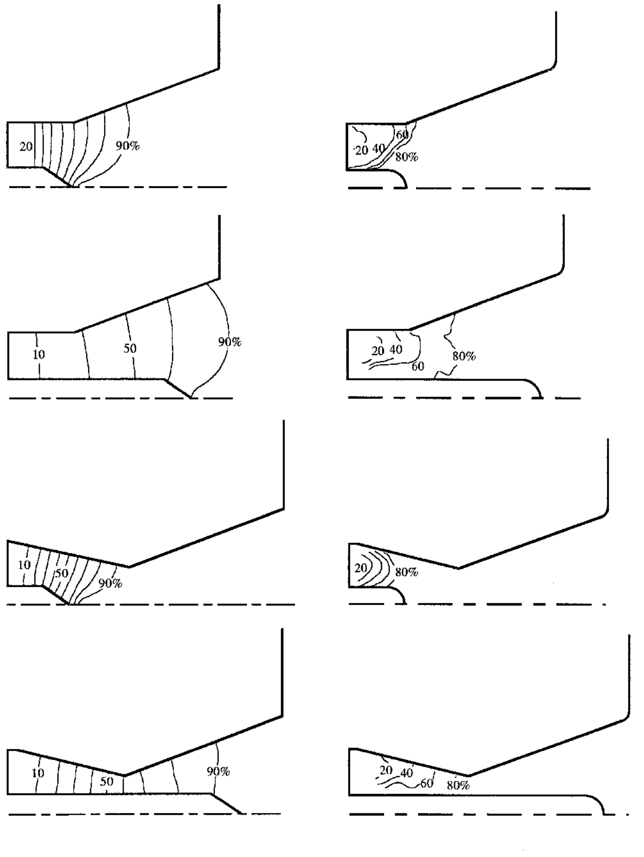

Calculation Experiment

Fig. 6 Comparison between measured and calculated current contour lines (J = 8 kA, $\dot{m}$ = 2.5 g/s).

along the centerline of the cathode, the principle of reflection was applied.

Results and Discussion

Validity of Calculation

There is an analytical solution for a one-dimensional and constant electrical conductivity problem,[14] with which one can validate the previously-mentioned time-marching finite difference TVD scheme, as well as the coupling condition of the electromagnetic and the fluid equations. As shown in Fig. 2, no severe discrepancy was found between the analytical and numerical solutions; deviation was within a few percent, which was mainly caused by numerical dissipation at steep physical gradients. In addition, mass conservation was preserved very well; error was less than 1% with the largest deviation 5% at the inlet.

50×30 grids were used for two-dimensional calculations. Numerical accuracy was investigated by examining the solutions for several variables on both coarse and fine grids. Studies of temperature, axial velocity, and plasma density indicated typical fractional error estimates of roughly 7% based on Richardson extrapolation.[15] The fractional error estimate for the magnetic flux density was less than 1%.

For the formula of electrical conductivity, we used Eq. (13). At a given operational condition, the value of electrical conductivity in the discharge chamber is almost constant everywhere except near the inlet and outlet where Joule heating becomes dominant. Hence, if one introduces a representative value of electrical conductivity, the flowfield can be determined. However, because the electric conductivity itself must be determined from the system of equations self-consistently, a predetermined conductivity will lead to a large error.

Flowfield Comparison

Calculated current contours, temperature, and plasma density distributions are plotted and compared with experimental data in Fig. 3. The calculated current attachment is different from the experimental data. The skewed current attachment to the cathode for the actual flow is attributed to the tensor conductivity near the electrode, which is not included in this simulation.

For the flow variables, temperature and density, both calculated and measured distributions agree fairly well, even in the simplified model. A remarkable temperature rise was observed near the cathode tip for each case; however, quantitatively, the calculated temperatures in the electrode barrel and near the cathode tip are high compared to measured temperatures. The calculated temperature is twice as high as the measured temperature in the interelectrode region, and reaches an unrealistic high value at the cathode tip. This will be attributed to perfect gas treatment in the simulation. In the actual flow, the ionization effect will absorb some of the power deposition and cool the flow.

Flow near the Cathode Tip

In MPD flowfield, M_m describes the flowfield well, while the ordinary aerodynamic Mach number appears only in the numerical procedure of the TVD scheme, but has no physical meaning. This is because the propagating disturbance in the MHD framework is not the gasdynamic sonic wave, but the

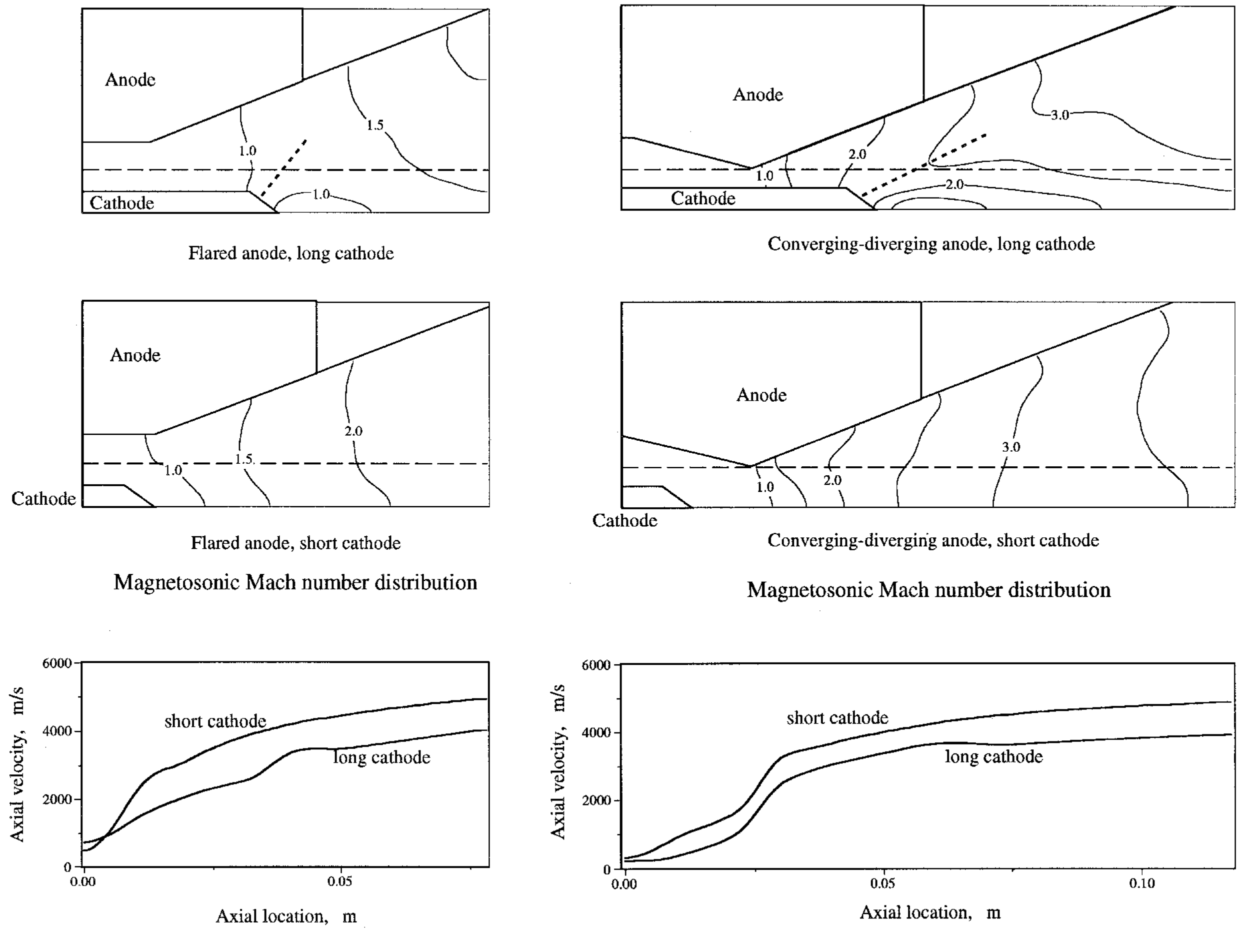

a) Axial velocity distribution at dotted lines b) Axial velocity distribution at dotted lines

Fig. 7 Magnetosonic Mach number distribution and axial velocity distribution; $J = 8$ kA, $\dot{m} = 2.5$ g/s: a) flared anode and b) converging–diverging anode configurations.

magnetosonic wave.[16] The only exception is the sonic singularity in a purely one-dimensional MPD flow.[14,17]

We now focus on the flowfield near the short cathode shown in Fig. 4. As J increases, the flow near the cathode tip, and accordingly, the magnetosonic Mach number distribution, changes its features. An oblique shock emerging near the tip of the cathode for the flow ($J = 1$ kA) disappears at $J = 4$ kA because of the heating effect, and the value of M_m at the tip remains below unity. At larger J, enhanced electromagnetic acceleration moves the magnetosonic transition toward the upstream region and supermagnetosonic flow toward the tip of the cathode again forms a weak oblique shock, as represented by the broken line in Fig. 4.

The MHD shock numerically predicted should be observed as a density jump. From the Mach–Zehnder interferometry of the 2D–MPD in Fig. 5, a very small density jump was found near the corner of the cathode. Unlike an oblique shock for cold flow, it is very weak. Therefore, it is very difficult to assert the existence of an MHD shock wave, and the calculated density rise behind the weak shock, which may exist, is very small.

Dependence on Electrode Geometry

The dependence of the MPD discharge on its electrode configuration is shown in Fig. 6. By adopting the short cathode, the discharge is restricted to the upstream region of the discharge chamber, which also changes the location of the magnetosonic passage. The location of the magnetosonic transition is hereafter referred to as the magnetosonic line. Figure 7 depicts magnetosonic Mach number distributions with their axial velocity profiles. As shown in Fig. 7a, a magnetosonic line $M_m = 1$ is located at the downstream region of the cathode tip for the short cathode configuration, whereas it is in the upstream of the cathode tip for a long cathode.

Different acceleration patterns of the two cathode configurations are explained analogously to gasdynamic flow with heat addition. It is known that the energy exchange with the gasdynamic flow has the effect of squeezing or expanding the cross-sectional area of the nozzle; thermal deposition into a subsonic region leads to efficient energy conversion from thermal to kinetic energy. In the MPD flow, thermal input into a submagnetosonic region results in acceleration, whereas thermal input into a supermagnetosonic region results in deceleration. The flow near the tip for the short cathode in Fig. 7a is submagnetosonic and the plasma is smoothly and efficiently accelerated while passing through the magnetosonic line. On the contrary, the thermal deposition at the cathode tip cannot be recovered in the case of the long cathode; moreover, thermal input into the supermagnetosonic region forms an MHD shock emerging from the cathode tip, which prevents smooth acceleration. MPD arcjets cannot avoid a discharge concentration at the end of the channel, where Joule heating becomes dominant. By adopting a short cathode configuration, the thermal deposition region is shifted into the upstream submagnetosonic region, resulting in efficient recovery of the thermal energy.

For the case of the converging–diverging configuration in Fig. 7b, the same explanation is applicable but the magnetosonic line is fixed at the throat, not only for this case, but also for a wide range of operational conditions.

Thrust Comparison

We compare the two-dimensional numerical results with experimental data. Thrust data are plotted in Fig. 8 for $\dot{m} = 2.5$ g/s. The predicted thrust agrees fairly well with the experimental data and this simulation code can therefore be considered to evaluate both electromagnetic and thermal acceleration. Comparisons of current contours exhibit differences only near the electrodes, thereby assuring the validity of the predicted axial component of the electromagnetic thrust. However, the calculated thermal thrust contribution, defined as the difference between measured and calculated thrust, is considered to show only the trend resulting from a wrong estimation of the thermal field obtained by this model: neglect of the ionization effect will lead to wrong temperature and plasma density; also, the radial component of the electromagnetic force near the cathode surface forms a radial profile of temperature and plasma density, which cannot be predicted in this simulation. For the case of the converging–diverging configuration, the deviation of the calculated thrust from the measured one becomes larger as J increases, leading to an overestimation of the thrust. This implies that the thermal energy input into the converging region is very efficiently used when the converging–diverging anode is adopted. In the case of the flared anode, both the short and long cathode geometry resulted in nearly the same thrust characteristics. The deviation of the calculated thrust for the long cathode and flared anode must be attributed to the insulator nozzle extended from the anode end recovering the thermal energy into the cathode tip, just like in the short cathode case. However, it cannot convert thermal energy into kinetic energy as efficiently as observed in the transmagnetosonic acceleration achieved in the short cathode configuration. As J increases, the thrust takes almost the same value for the short and long cathode, because the movement of the magnetosonic line toward the upstream region makes both flowfields neary equal, and a shock wave appears. In the actual flow, the long cathode with flared anode configuration fails to recover thermal energy unless the insulator nozzle is attached, as provided in the numerical simulation. With all of these results taken into consideration, one can say that the short cathode configuration always produces larger thrust compared to the one with the long cathode, by virtue of enhancing aerodynamic thrust.

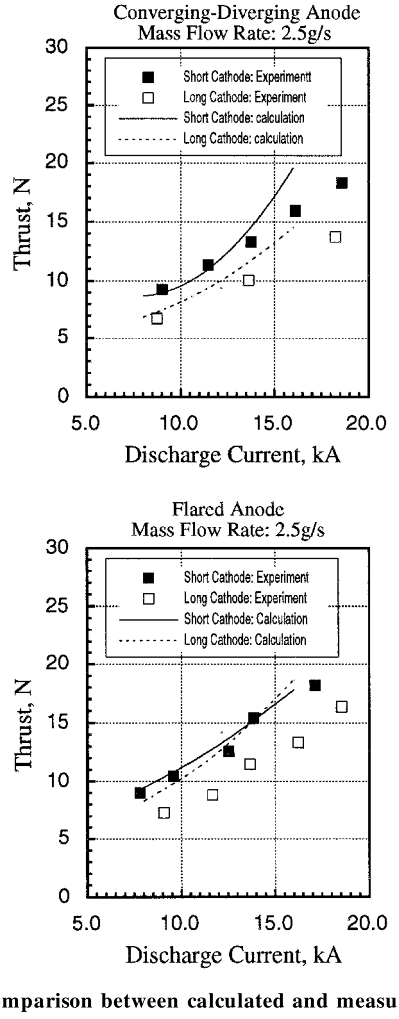

Fig. 8 Comparison between calculated and measured thrust.

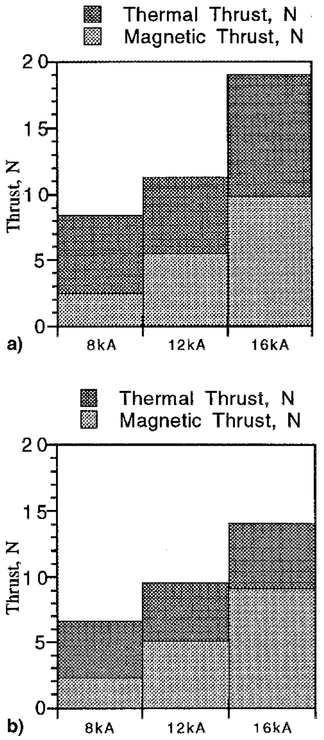

Fig. 9 Calculated electrothermal and electromagnetic thrust component; converging–diverging anode: a) short and b) long cathode, $\dot{m}$ = 2.5 g/s.

Despite the good simulation of thrust data, the calculated discharge voltage differs from experimental data, even if we add a sheath drop voltage estimated from the experiment data. The voltage is derived from the idealistic numerical model, taking into account only the power spent in the electromagnetic acceleration and Joule heating.

Efficient Mechanism of Acceleration

In Fig. 9, the calculated thrust is broken into two parts: electromagnetic blowing thrust and electrothermal thrust. The former is the axial Lorentz force, the latter is calculated as the difference between the total thrust and the magnetic thrust. The electromagnetic thrust depends mostly on the discharge current and does not depend on other parameters such as electrode geometry. Therefore, the electromagnetic thrust for the calculated configurations is almost the same for the same discharge current. Only the electrothermal thrust explains the remarkable difference. In particular, for small $J^2/\dot{m}$, the fraction of thermal thrust exceeds 50% of the total; hence, enhancing thermal thrust with the short cathode geometry is key in the lower *Isp* range. At larger $J^2/\dot{m}$, electromagnetic thrust becomes dominant, and the flowfield includes an MHD shock, except for the short cathode configuration with the converging–diverging anode. The thermal-energy recovery using an extended insulation nozzle is still valid, but it is not as efficient as transmagnetosonic acceleration. It is concluded that from the viewpoint of an idealized thermal and electromagnetic hybrid accelerator, the short cathode configurations are superior to the long cathode configurations. Except with the converging–diverging anode configuration, the short cathode geometry loses its superiority in electromagnetic-dominant operations because of the appearance of a shock wave.

Conclusions

Numerical simulations of a two-dimensional MPD arcjet were conducted to explain the thrust characteristics. The model based on MHD equations showed that in the practical *Isp* range, the MPD arcjet changes its features from electrothermal to electromagnetic operation; hence, enhancing electrothermal thrust becomes important. Two types of cathode configurations were compared: short and long cathodes. The short-cathode configurations, which enhance the electrothermal thrust through transmagnetosonic acceleration, is superior to the long cathode configurations, regardless of the anode shape.

The MPD flowfield cannot avoid excess heating at the cathode tip. Because of the large electromagnetic force in the MPD channel, the MPD flow becomes supersonic. Hence, supersonic heating and compression near the cathode tip is likely to cause an oblique shock. Judging from the distribution of the magnetosonic Mach number, the cathode tip region is close to magnetosonic conditions. The induced shock is very weak or unobservable; however, the short cathode configuration produces large aerodynamic thrust, while the long cathode configurations cannot recover the thermal deposition on the cathode tip, where supermagnetosonic heating occurs. When the long cathode was employed, numerical simulation showed that thermal energy can be recovered by an extended insulation nozzle, which is also shown to be effective to achieve large thrust.

References

[1] Auweter-Kurtz, M., Kurtz, H. L., Schrade, H. O., and Sleziona, P. C., "Numerical Modeling of the Flow Discharge in MPD Thrusters," *Journal of Propulsion and Power*, Vol. 5, No. 1, 1989, pp. 49–55.

[2] LaPointe, M. R., "Numerical Simulation of Self-Field MPD Thrusters," AIAA Paper 91-2341, June 1991.

[3] Park, W. T., and Choi, D. I., "Two-Dimensional Model of the Plasma Thruster," *Journal of Propulsion and Power*, Vol. 4, No. 2, 1988, pp. 127–132.

[4] Chanty, J. M. G., and Martinez-Sanchez, M., "Two-Dimensional Numerical Simulation of MPD Flows," AIAA Paper 87-1090, May 1987.

[5] Niewood, E. H., and Martinez-Sanchez, M., "Quasi-One-Dimensional Numerical Simulation of Magnetoplasmadynamic Thruster," *Journal of Propulsion and Power*, Vol. 8, No. 5, 1992, pp. 1031–1039.

[6] Miller, S., and Martinez-Sanchez, M., "Viscous and Diffusive Effects in MPD Flows," AIAA Paper 90-2606, July 1990.

[7] Niewood, E. H., and Martinez-Sanchez, M., "The Hall Effect in a Numerical Model of MPD Thrusters," 22nd International Electric Propulsion Conf., IEPC91-099, Oct. 1991.

[8] Sleziona, P. C., Auweter-Kurtz, M., and Schrade, H. O., "Computation of MPD Flows and Comparison with Experimental Results," *International Journal for Numerical Methods in Engineering*, Vol. 34, No. 3, 1992, pp. 759–771.

[9] Funaki, I., Toki, K., and Kuriki, K., "Effect of Electrode Configuration on the Performance of a Two-Dimensional Magnetoplasmadynamic Arcjet," *Journal of Propulsion and Power* (to be published).

[10] Toki, K., Sumida, M., and Kuriki, K., "Multichannel Two-Dimensional Magnetoplasmadynamic Arcjet," *Journal of Propulsion and Power*, Vol. 8, No. 1, 1992, pp. 93–97.

[11] Nakayama, T., and Toki, K., and Kuriki, K., "Quantitative Imaging of Magnetoplasmadynamic Arcjet," *Journal of Propulsion and Power*, Vol. 8, No. 6, 1992, pp. 1217–1223.

[12] Thompson, J. F., Warsi, Z. U. A., Mastin, C. W., "Numerical Grid Generation," Elsevier, Amsterdam, 1985.

[13] Yee, H. C., "A Class of High-Resolution Explicit and Implicit Shock-Capturing Method," NASA TM101088, Feb. 1989.

[14] King, D. Q., "Magnetoplasmadynamic Channel Flow for Design of Coaxial MPD Thrusters," Ph.D. Dissertation, Princeton Univ., Princeton, NJ, 1981.

[15] Roache, P. J., "Perspective: A Method for Uniform Reporting of Grid Refinement Studies," *Journal of Fluids Engineering*, Vol. 116, No. 3, 1994, pp. 405–413.

[16] Kuriki, K., and Nakayama, T., "Magnetosonic Condition in Magnetoplasmadynamic Flow," *Journal of Propulsion and Power*, Vol. 8, No. 6, 1992, pp. 1208–1211.

[17] Martinez-Sanchez, M., "Structure of Self-Field Accelerated Plasma Flows," *Journal of Propulsion and Power*, Vol. 7, No. 1, 1991, pp. 56–64.